ACS APPLIED MATERIALS & INTERFACES

Research Article

www.acsami.org

Photoelectrochemical Properties of Cadmium Chalcogenide-Sensitized Textured Porous Zinc Oxide Plate Electrodes

Saim Emin,*[†] Mattia Fanetti,[†] Fatwa F. Abdi,[‡] Darja Lisjak,[§] Matjaz Valant,[†] Roel van de Krol,[∇] and Bernard Dam[‡]

[†]Materials Research Laboratory, University of Nova Gorica, SI-5000 Nova Gorica, Slovenia

[‡]Materials for Energy Conversion and Storage (MECS), Department of Chemical Engineering, Delft University of Technology, 2600 GA Delft, The Netherlands

[§]Department for Materials Synthesis, Jožef Stefan Institute, 1000 Ljubljana, Slovenia

[∇]Institute for Solar Fuels, Helmholtz-Zentrum Berlin für Materialien und Energie GmbH, Hahn-Meitner-Platz 1, 14109 Berlin, Germany

Supporting Information

ABSTRACT: We report the photoelectrochemical (PEC) performance of textured porous ZnO and CdX-coated ZnO films (X = S, Se). Porous ZnO films were grown with a platelike morphology on F-doped SnO_2 (FTO) substrates. The growth of ZnO films involves a two-step procedure. In the first step, we electrochemically grew simonkolleite ($Zn_5(OH)_8Cl_2{\cdot}H_2O$) plate films. Annealing of the simonkolleite at 450 °C results in textured porous ZnO films. The as-obtained porous ZnO electrodes were then used in PEC studies. To increase the light-harvesting efficiency, we sensitized these ZnO electrodes with CdS and CdSe quantum dots, using the so-called "successive ion layer adsorption and reaction (SILAR) method". As expected, the photocurrent density systematically increases when going from ZnO to ZnO/CdS to ZnO/CdSe. The highest photocurrent, ~3.1 mA/cm^2 at 1.2 V vs RHE, was obtained in the CdSe-sensitized ZnO electrodes, because of their enhanced absorption in the visible range. Additionally, quantum efficiency values as high as 90% were achieved with the textured porous ZnO films. These results demonstrate that both CdS and CdSe-sensitized textured porous ZnO electrodes could be potentially useful materials in light-harvesting applications.

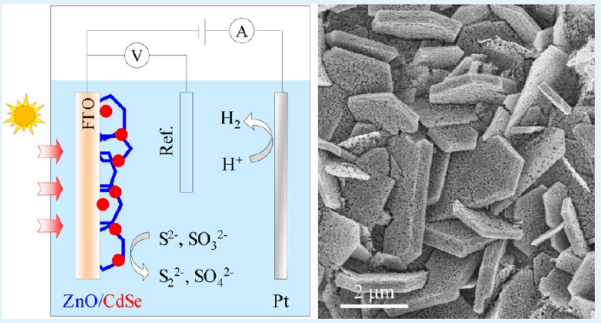

KEYWORDS: *SILAR, textural porosity, photoelectrochemical cell, quantum dot, sensitization*

1. INTRODUCTION

In recent years, it has been demonstrated that ZnO nanostructured electrodes are very useful in photocatalysis,[1] dye-sensitized solar cells (DSSCs),[2] and in photoelectrochemical cell (PEC)[3,4] studies. It has been shown that electrodeposition is a convenient and fast method for the preparation of ZnO thin films.[5,6] Aligned ZnO arrays such as nanowires and nanosheets are particularly suited for light-harvesting applications, since they exhibit the ideal morphology for providing a path for the photogenerated carriers.[7−9] In addition to charge carrier transport, porosity is another crucial factor that greatly influences the chemical reaction rate that occurs at the surface of ZnO electrodes. A typical example of this can be seen in the case of ZnO electrodes used in DSSC studies.[10]

Although ZnO can be used as light-harvesting material on its own, it has limited absorption in the visible (VIS) region. One way to extend the light harvesting ability of ZnO in the VIS-region is to sensitize it with short-band-gap semiconductor quantum dots (QDs) such as CdS,[11,12] CdSe,[13] CdS/CdSe[14,15] and CdTe.[16,17] QDs are a class of semiconductor nanomaterials that shows tunable absorption due to the so-called quantum confinement effect, and they are often used as sensitizers in solar cells[18,19] or in photocatalytic systems.[20] QD sizes can be tuned over a wide range, from 2 nm to 30 nm, depending on the type of material from which they are composed.[21,22]

There are different strategies for attaching QDs on the surface of metal oxide electrodes, and these can be classified into two groups: assembly of presynthesized QDs and direct growth.[23,24] The use of presynthesized QDs allows one to maintain low size distribution, high photoluminescence, and control over the QDs morphology. For direct growth, chemical bath deposition (CBD)[25] and successive ion layer adsorption and reaction (SILAR)[26] methods are preferred, because of their simplicity and convenience. The SILAR method has been used to decorate ZnO electrodes with various types of QDs for use in PEC studies.[27] The most-studied ZnO-based PEC systems

Received: November 29, 2012
Accepted: January 16, 2013
Published: January 16, 2013

are those that contain QDs with binary compositions, such as CdS,[28,29] CdSe,[30−32] CdTe,[33] or ternary compositions such as $CuInS_2$,[34] and ZnCdS.[35] The metal oxide electrode, usually *n*-type semiconducting photoanodes, is often a nanostructured porous film or nanowire array where the thickness of the films ranges from 100 nm to 30 μm.[36,37] The great interest in CdX-sensitized ZnO electrodes (X = S, Se) arises from the fact that these systems are applied both in photovoltaics (PV)[38−41] and for light-induced hydrogen evolution.[42−44] Although there are studies on ZnO and CdX-sensitized ZnO array electrodes, there are no reports on the application of ZnO plates in PEC studies. The advantage of using porous ZnO plate electrodes in PEC is 3-fold. First, the porous structure of ZnO serves as a scaffold for efficient loading of CdX QDs; second, the ZnO plates shows light scattering features; and third, the platelike structure allows efficient electron transport, which was demonstrated by illumination of the ZnO electrodes from the front and back sides.

Here, we report the application of cadmium chalcogenide-sensitized textured porous ZnO plate electrodes for PEC studies in the presence of sacrificial sulfide (S^{2-}) and sulfite (SO_3^{2-}) ions. The smooth $Zn_5(OH)_8Cl_2{\cdot}H_2O$ plate electrodes are first fabricated by using electrochemical deposition, following our previously reported procedure.[45] The structural transformation of $Zn_5(OH)_8Cl_2{\cdot}H_2O$ to ZnO was performed by heat treatment at 450 °C. These ZnO plates were then sensitized with CdS and CdSe QDs, using the SILAR method. Although the experimental conditions for the growth of ZnO plates are known from previous reports, it is highly valuable to evaluate the potentials of this system in PEC studies with the possibility for H_2 evolution. Transmission electron microscopy (TEM) images revealed the attachment mode of CdX on the surface of the ZnO electrodes. As a result of the sensitization, the onsets of absorption as well as the photocurrent are red-shifted up to ∼660 nm for CdSe-sensitized ZnO electrodes. Incident photon-to-current efficiency (IPCE) studies showed that both ZnO and CdX-sensitized ZnO electrodes exhibit IPCE values as high as 90%. These results thus confirm that both the light harvesting and the charge separation are very efficient, and CdS- and CdSe-sensitized ZnO nanostructured electrodes are promising for PEC applications.

2. EXPERIMENTAL PROCEDURES

Chemicals. Zinc chloride ($ZnCl_2$, 99%), hydrogen peroxide (H_2O_2, 98%), cadmium nitrate ($Cd(NO_3)_2$, 97%), selenium powder (Se, 99.9%), sodium borohydride ($NaBH_4$, 97%), ethanol (EtOH, 99%), sodium sulfite (Na_2SO_3, 99%), and sodium sulfide (Na_2S, 99%) were purchased from Sigma−Aldrich and used as-received.

Fabrication of ZnO and ZnO/CdX Electrodes. ZnO working electrodes were prepared in a cell with a two-electrode configuration. F-doped SnO_2-coated glass substrates (Geomatec, Japan) with dimensions of ∼6 cm × 1.4 cm were used as both the anode and the cathode. The deposition of $Zn_5(OH)_8Cl_2{\cdot}H_2O$ plates was carried out at 75 °C in an aqueous solution of 0.1 M $ZnCl_2$ and 0.2 M H_2O_2. By applying a DC voltage of 2.6 V for 30 min, we were able to deposit a ∼6-μm-thick $Zn_5(OH)_8Cl_2{\cdot}H_2O$ film on the cathode. Porous ZnO plates have been obtained by annealing the $Zn_5(OH)_8Cl_2{\cdot}H_2O$ film at 450 °C for 30 min (in air). Sensitization of ZnO electrodes with CdS and CdSe QDs was achieved using the SILAR method. For the ZnO/CdSe electrodes, one dipping cycle consists of immersing the ZnO electrodes in two different ethanol solutions (0.05 M $Cd(NO_3)_2$ and 0.05 M Na_2Se) for 1 min each. Preparation of 0.05 M Na_2Se was achieved by dissolving Se (0.19 g, 2.5 mmol) powder in 0.1 M $NaBH_4$ ethanol solution (50 mL) under N_2 atmosphere. Following each immersion, the electrodes were rinsed for 1 min using ethanol to remove any excess of precursor solution. This was repeated for five cycles under N_2 atmosphere. In the case of ZnO/CdS electrodes, 0.05 M Na_2S solution was used instead of the sodium selenide solution and the SILAR was carried out in air. Electrical contacts to the electrodes were made using a silver wire and graphite conductive adhesive (Alfa Aesar, U.K.).

Characterizations and Measurements. The phase composition of the as-prepared products was determined using a PANalytical X-ray diffractometer with Cu Kα radiation (λ = 1.54 Å). The morphology of the structures was studied with a Supra 40 scanning electron microscopy (SEM) system (Carl Zeiss) equipped with a field-emission electron column (Gemini) and coupled to an energy dispersive X-ray spectrometer (EDXS; EDAX). Transmission electron microscopy (TEM) studies were conducted using a JEM-2100 system (JEOL) equipped with EDXS. Diffuse reflectance spectra were recorded on a Lambda 650 UV−vis spectrophotometer (Perkin−Elmer). PEC measurements were done in a three-electrode configuration in an aqueous mixture of 0.1 M Na_2S and 0.1 M Na_2SO_3 solution (pH 13), where the electrode area was defined to be 0.283 cm^2. The potential of the working electrode was controlled by a potentiostat (EG&G PAR283). A coiled Pt wire and an Ag/AgCl electrode (XR300, Radiometer Analytical) were used as the counter and reference electrodes, respectively. Potentials vs Ag/AgCl were converted to the reversible hydrogen electrode (RHE) scale by the Nernst equation $E_{RHE} = E_{Ag/AgCl} + E^0_{Ag/AgCl} + 0.059pH$.[46] In this equation, $E^0_{Ag/AgCl}$ was 0.1976 V at 25 °C, and $E_{Ag/AgCl}$ was the measured potential against the Ag/AgCl reference electrode. Chopped-light voltammetry measurements were performed with a scan rate of 10 mV/s and a shutter frequency of 0.1 Hz. White-light photocurrent measurements were performed under simulated AM1.5 solar illumination (100 mW/cm^2) with a Newport Sol3A Class AAA solar simulator (type 94023A-SR3). Monochromatic photocurrents were measured with a 300-W xenon arc lamp (Oriel, Model 6259) coupled into a grating monochromator (Acton SpectraPro 150i). An electronic shutter (Uniblitz LS6) was used and a long-pass colored glass filter (Schott, 3 mm thick) was placed between the monochromator and the sample to remove second-order diffracted light. The shutter was actuated with a frequency of 0.05 Hz, and the photocurrent was taken as the difference between the current when the shutter is opened and closed (integration time = 3 s and step size ≈ 1.5 nm). The incident photon-to-current efficiency (IPCE) is calculated based on the formula[47]

$$\mathrm{IPCE}\ (\%) = \frac{1240 \times J(\mathrm{mA/cm^2})}{P_{\mathrm{light}}(\mathrm{mW/cm^2}) \times \lambda(\mathrm{nm})} \times 100 \quad (1)$$

where J is the steady-state photocurrent density at a specific wavelength and λ is the wavelength of the incident light. P_{light} is the light intensity for wavelength λ at the film surface. The illumination intensity from the xenon source was measured with a calibrated photodiode (Ophir PD300-UV). Electrochemical impedance spectroscopy (EIS) was performed by connecting a Solartron model 1260 Frequency Response Analyzer (FRA) to the potentiostat. The measurements were performed using a perturbation amplitude of 10 mV at open circuit potential under AM1.5 illumination.

3. RESULTS AND DISCUSSION

Preparation of Porous ZnO Plate Electrodes. The preparation of the nanoporous ZnO plate electrodes can be divided in two stages. The first stage involves the electrochemical growth of $Zn_5(OH)_8Cl_2{\cdot}H_2O$ crystals on the FTO electrode. The second-stage includes structural transformation of $Zn_5(OH)_8Cl_2{\cdot}H_2O$ into ZnO at elevated temperatures. The growth mechanism of $Zn_5(OH)_8Cl_2{\cdot}H_2O$, which takes place during the first stage, can be represented by the following equations that occur at the cathode surface:[48,49]

$$H_2O_2 + 2e^- \rightarrow 2OH^- \quad (2)$$

$$5Zn^{2+} + 8OH^- + 2Cl^- + H_2O \rightarrow Zn_5(OH)_8Cl_2{\cdot}H_2O \quad (3)$$

Reaction 2 locally increases the pH, which causes the precipitation of a zinc oxyhydride phase, accompanied by the incorporation of Cl^- ions to form crystalline $Zn_5(OH)_8Cl_2{\cdot}H_2O$. Parallel to reaction 2 at the counter electrode, the Cl^- ion is oxidized to Cl_2 (E^0 = −1.36 V vs normal hydrogen electrode, NHE). We reproducibly grew $Zn_5(OH)_8Cl_2{\cdot}H_2O$ crystals from aqueous solutions at 75 °C by modifying the experimental conditions given in ref 45. Figure 1

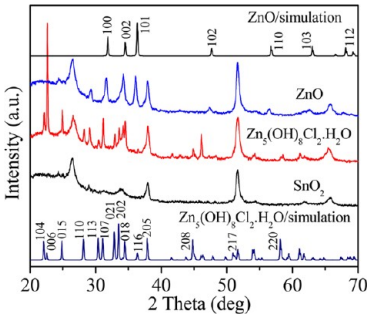

Figure 1. XRD patterns of $Zn_5(OH)_8Cl_2{\cdot}H_2O$, SnO_2, and ZnO phases. The FTO/glass substrate is given as SnO_2. In the bottom and at the top are shown the simulated diffractograms of $Zn_5(OH)_8Cl_2{\cdot}H_2O$ and ZnO phases that are taken from reference PDF cards.

shows a typical XRD pattern of the $Zn_5(OH)_8Cl_2{\cdot}H_2O$ crystals on the FTO substrate. A good match with the simonkolleite reference pattern ($Zn_5(OH)_8Cl_2{\cdot}H_2O$, PDF Card No. 00-007-0155)[50] was observed in terms of peak positions. However, the same is not true for the peak intensities. The variations in the peak intensity showed a significant preferential growth in the crystals. The distinct change occurred in the intensity of the (006) diffraction peak, which indicates that the crystals are growing preferentially along the [001] direction. The [001] direction, in our case, is along the basal plane of a single $Zn_5(OH)_8Cl_2{\cdot}H_2O$ plate. Heat treatment of the $Zn_5(OH)_8Cl_2{\cdot}H_2O$ crystals at 450 °C causes thermal decomposition and conversion of the crystals into porous ZnO plates. As shown in Figure 1, the XRD pattern of the ZnO residue after heating corresponds well to the ZnO zincite reference pattern (PDF Card No. 01-089-0511).[51] The lattice parameters, calculated with Rietveld refinement, agree with the zincite values from the reference card (a = 3.252 nm (2), b = 5.216 nm (3)). The calculation of the crystallite size from the diffraction peak broadening ((101) plane), using Scherrer's formula,[52] give values of ∼20 to 30 nm and indicates that the system consists of randomly distributed ZnO nanodomains. The thermal decomposition of $Zn_5(OH)_8Cl_2{\cdot}H_2O$ is a multistage process. As the temperature increases water molecules are driven off. Above 170 °C, the anhydrous $Zn_5(OH)_8Cl_2$ further decomposes, yielding ZnO and $ZnCl_2$ phases. The decomposition steps can be represented by the following reactions:[53]

$$Zn_5(OH)_8Cl_2{\cdot}H_2O \xrightarrow{150\circ C} Zn_5(OH)_8Cl_2 + H_2O \quad (4)$$

$$Zn_5(OH)_8Cl_2 \xrightarrow{260\circ C} 4ZnO + ZnCl_2 + 4H_2O \quad (5)$$

$ZnCl_2$ is volatile at elevated temperatures and evaporates as the temperature increases to 450 °C. However, it is also possible that a small fraction of $ZnCl_2$ might hydrolyze to form ZnO and HCl.

SEM analysis shows that the as-synthesized film that completely covers the FTO substrate is made of randomly oriented hexagonal (or half-hexagonal) plates of $Zn_5(OH)_8Cl_2{\cdot}H_2O$ (Figure 2). These plates exhibit smooth surfaces and clearly defined edges. The typical width of the plates is in the 1−6 μm range, and their thickness is ∼50−300 nm. The plates grow from the FTO substrate along their fast-growing direction, i.e., the crystal [001] direction, as shown by XRD. The thermal decomposition of the $Zn_5(OH)_8Cl_2{\cdot}H_2O$

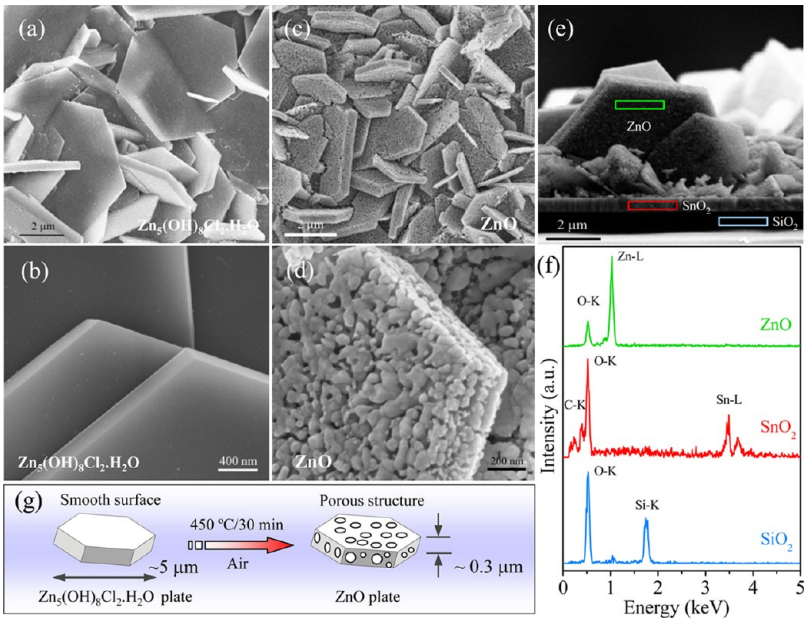

Figure 2. SEM images of (a,b) $Zn_5(OH)_8Cl_2{\cdot}H_2O$ and (c,d) ZnO plates at different magnifications viewed from the top. (e) Cross-sectional view of the ZnO film with (f) corresponding EDXS spectra of the substrate phases and ZnO plates. (g) Scheme showing the phase transformation of $Zn_5(OH)_8Cl_2{\cdot}H_2O$ to ZnO at 450 °C.

dx.doi.org/10.1021/am3027986 | ACS Appl. Mater. Interfaces 2013, 5, 1113−1121

crystals is associated with a loss of over 40% of mass, which must result in a change in the morphology. Interestingly, the general overall shape of the plates is retained during heat treatment, but their fine structure is changed. Figures 2c and 2d show the resulting porosity in such newly formed ZnO plates. The shape of pores within the ZnO network is irregular. The typical size of the pore is <100 nm (Figure 2d). Furthermore, EDXS analysis of ZnO plates (see Figures 2e and 2f) show that they are composed of only Zn and O. It should be noted that the density and orientation of ZnO plates could be greatly affected by the current density during growth (see the Supporting Information).

TEM images of ZnO agglomerates and a corresponding selected area electron diffraction (SAED) patterns are shown in Figure 3. These agglomerates are obtained after scratching the

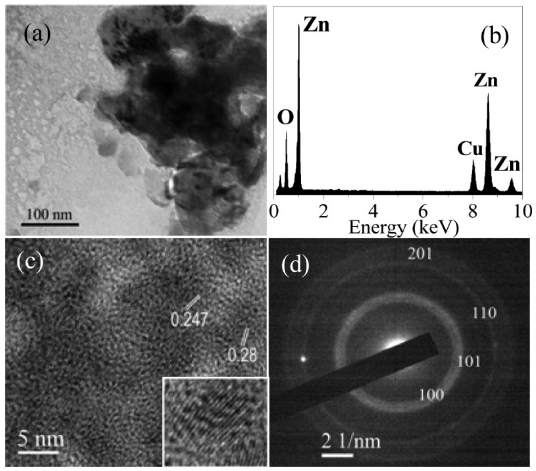

Figure 3. (a,c) TEM images of ZnO nanoparticles; (b) EDXS spectrum of ZnO taken from panel (a); and (d) SAED taken from panel (c). A copper grid is used as the substrate.

surface of ZnO plate electrode with a spatula. The composition of ZnO was confirmed by EDXS (Figure 3b) and its structure was indexed according to the hexagonal structure of ZnO space group *P*63*mc* (196) PDF Card No. 01-089-0511. TEM image taken at higher magnifications shows a netlike structure of the agglomerates (Figure 3c). This netlike structure consists of individual ZnO nanoparticles and is formed from crystallites of ~15 nm in diameter. Figure 3c shows some of the nanoparticles exhibiting crystal lattice fringes with a separation of 0.24 and 0.28 nm, which correspond to the (101) and (100) planes of ZnO. The corresponding SAED pattern also confirms that ZnO nanocrystals are randomly oriented and are very small as indicated by the presence of diffuse rings in the pattern (Figure 3d).

Preparation of CdX-Sensitized ZnO Plate Electrodes (X = S, Se). Since the as-synthesized ZnO plates are porous and have a wide range of pore sizes, one would expect them to show promise in PEC studies. Our detailed SEM analysis shows that the plates exhibit both mesopores (2−50 nm) and macropores (>50 nm). A high degree of porosity enhances the overall surface reaction kinetics and is likely to increase the photocurrent. The latter is presumably limited by the large band gap, which limits its light absorption in the VIS range. In order to extend its response to VIS light, it can be sensitized with either a dye molecule (e.g., N719)[54] or a low-band-gap semiconductor QDs[55] that shows photoactivity under VIS light. We chose the latter: ZnO sensitization with CdS and CdSe QDs. Figure 4 shows the diffuse absorption spectra of bare

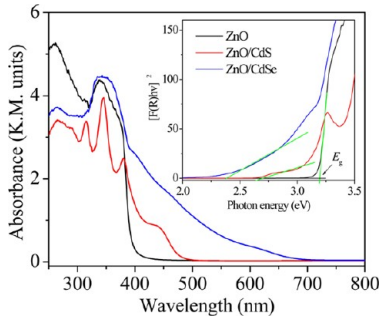

Figure 4. Diffuse absorbance spectra of the pure ZnO and CdX-sensitized ZnO plate electrodes. From the inset plot, the direct band gaps of the semiconductor materials are determined.

ZnO plates and those sensitized with CdS and CdSe QDs. From the inset plot, we determined the band gap (E_g) of the ZnO plates and found that E_g is 3.2 eV, much larger than the apparent band gap values obtained for the CdX (X = S, Se) QDs. The typical apparent band gaps of CdS and CdSe QDs are 2.4 and 2.7 eV, respectively. We notice that the estimation of CdX QDs band gap involves certain assumptions. First, we extrapolate only a part of the spectrum of ZnO/CdX plates (see inset in Figure 4) at longer wavelength assuming that this part is due to the CdX QDs. For example, in the spectrum of ZnO/CdSe plates, the extrapolation that yields the band gap of CdSe QDs includes the region between 2.5 eV and 2.8 eV. The apparent band gaps are much larger than the reported band gap values of 1.7 and 2.4 eV for bulk CdSe and CdS.[56] The increase in the band gaps are due to the quantum confinement effect, which is known to play a major role in small crystallites.[57] As a general trend, the pronounced absorption in the VIS region by the CdS or CdSe-sensitized ZnO electrodes is expected to increase the number of absorbed photons in these electrodes. In addition, the absorption above 400 nm is an indicator that CdS and CdSe sensitization takes place on ZnO electrodes, because the light absorption in the VIS region arises mainly from CdS and CdSe QDs.

Figure 5 shows TEM images of a ZnO/CdS sample. The entity in Figure 5a is an agglomerate of ZnO nanocrystals coated with CdS QDs. The SAED (inset in Figure 5a) of the agglomerate can be indexed with hexagonal ZnO and CdS structures (JCPDS File Card No. 89-2944; indices in brackets). Figure 5b shows the TEM image of the entity in Figure 5a, taken at a higher magnification. In the image, we observed two types of lattice fringes that correspond to various crystallographic planes. As shown with parallel lines, those lattice fringes are equal to 0.26 nm, which corresponds to the (002) plane of ZnO, and the lattice spacing is equal to 0.20 nm, which corresponds to the (110) plane of CdS. The EDXS confirms the expected chemical composition with peaks of Zn, Cd, O, and S. The typical sizes of CdS QDs are on the order of ~5 nm.

Detailed SEM observations of the CdS- and CdSe-sensitized ZnO electrodes show that the QDs effectively cover the surface of ZnO plates (see the Supporting Information). Figures 6a and 6b show SEM images of the ZnO plates before and after coating with CdSe QDs. The textural porosity of the ZnO plates allows one to form a dense coating with either CdS or CdSe QDs. The pore sizes, which are in the order of ~100 nm,

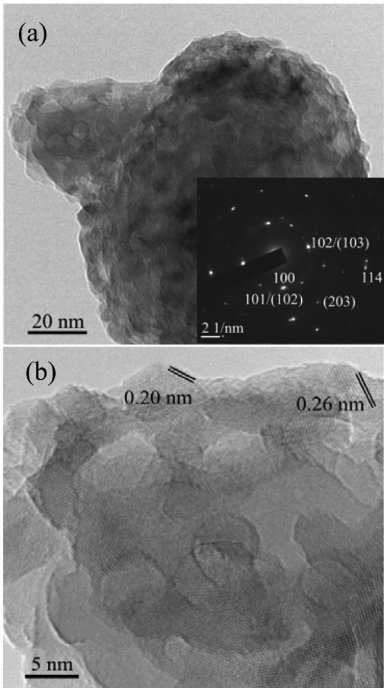

Figure 5. (a) TEM image of a ZnO/CdS sample and corresponding SAED pattern (the indices given in brackets correspond to the CdS while the others correspond to ZnO). (b) Magnified TEM image of the ZnO/CdS sample shown in panel (a).

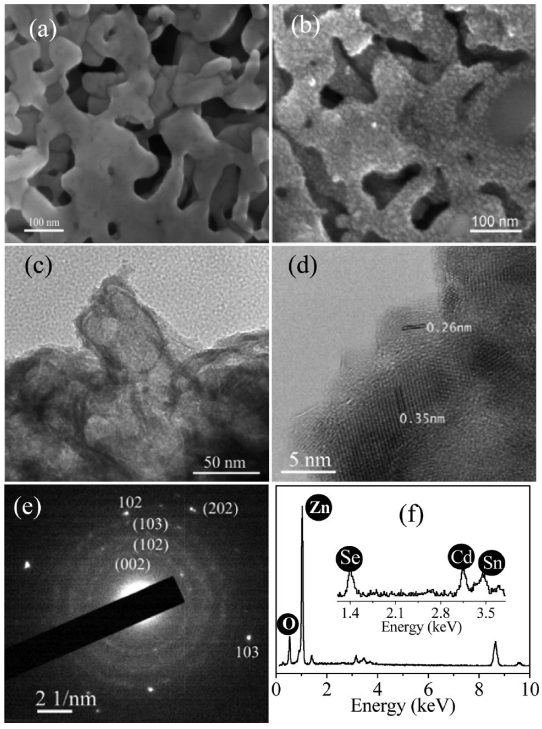

Figure 6. SEM images of ZnO plate electrodes (a) before and (b) after sensitization with CdSe QDs. (c,d) TEM images of ZnO/CdSe at different magnifications. (e) SAED taken from the object shown in panel (c) (indices given in brackets correspond to CdSe, while others correspond to ZnO). (f) EDXS taken by SEM from a CdSe-sensitized ZnO plate.

allows an efficient loading of QDs with typical sizes of ~5 nm. Note that, in this case, we selected an area on the ZnO plate surface that has larger pores than the ZnO plates shown in Figure 2. EDXS studies confirmed the presence of intense signals for Zn and O. In the spectra, there are also weak signals from Cd and Se, indicating that the CdSe QDs are successfully loaded onto the porous ZnO plates (Figure 6f). The low intensity of the metal chalcogenide elements compared with that of Zn and O is due to the fact that the amount of CdSe is relatively low, compared to the total mass of ZnO. The agglomerate shown in the TEM images (Figures 6c and 6d) is composed of nanocrystallites, as suggested from the corresponding SAED pattern (Figure 6e). The diffraction rings can be indexed with two structures: the zincite ZnO (JCPDS File Card No. 36-1451) and the hexagonal CdSe (JCPDS File Card No. 77-0046); the corresponding indices are given in brackets. The coexistence of the two types of crystallite is also suggested from Figure 6e, where the nanocrystals with lattice fringes separated by 0.26 and 0.35 nm are shown. These spacings correspond to the (002) crystal planes of ZnO and CdSe, respectively.

Photoelectrochemical Properties of CdS- and CdSe-Sensitized ZnO Electrodes. Large photoanode surface areas, rapid electron transport paths, and high optical absorption are significant in producing efficient ZnO-based PEC cells for photovoltaic or photoelectrochemical applications. Since our ZnO plate films potentially fulfill all these requirements, PEC performance characterization was carried out. Figure 7a shows linear sweep voltammograms (LSVs) of various electrodes under chopped AM1.5 illumination. While pure ZnO plates show a photocurrent density (J) of only ~0.4 mA/cm^2 at 1.2 V (vs RHE), the electrodes composed of CdS- and CdSe-sensitized ZnO showed much higher values (on the order of ~2.0 and ~3.1 mA/cm^2, respectively). The higher photocurrent for CdS- and CdSe-sensitized ZnO electrodes is consistent with their respective IPCE values, as shown in Figure 7b. The onset of the IPCE spectra is shifted from 420 nm for ZnO to 520 and 650 nm for CdS- and CdSe-sensitized ZnO electrodes, respectively. This shift is also consistent with the observed absorption edge shift in Figure 4, indicating that the photocurrent improvements are mainly caused by the higher absorption in the VIS region.

We should note that the photocurrents reported above are obtained under back-side illumination, i.e., light is incident via the transparent conducting electrode. Figure 7c compares the photocurrent densities vs potential of ZnO/CdSe plates under front- and back-side illumination with simulated sunlight. We found that the ZnO/CdSe electrodes illuminated in back configuration always show much higher photocurrents. This is true for all wavelengths, as shown in the IPCE spectra of Figure 7d. For mesoporous thin film photoanodes, a difference between front- and back-side illumination may indicate electron transport limitations.[58,59] For many systems, illumination from the back side gives higher IPCE values, because of the fact that the collection of photogenerated electrons is more efficient in such cases.[60] Upon front-side illumination of the ZnO film, most of the charge carriers are generated relatively far from the FTO substrate, so the electrons are subject to more recombinations during the transport through the film, which consequently gives lower IPCE values. Such a pronounced difference is a clear indication that the overall photoresponse is limited by the electron transport properties of the material. We also checked the possibility if the light scattering could contribute to the observed difference of IPCE spectra in

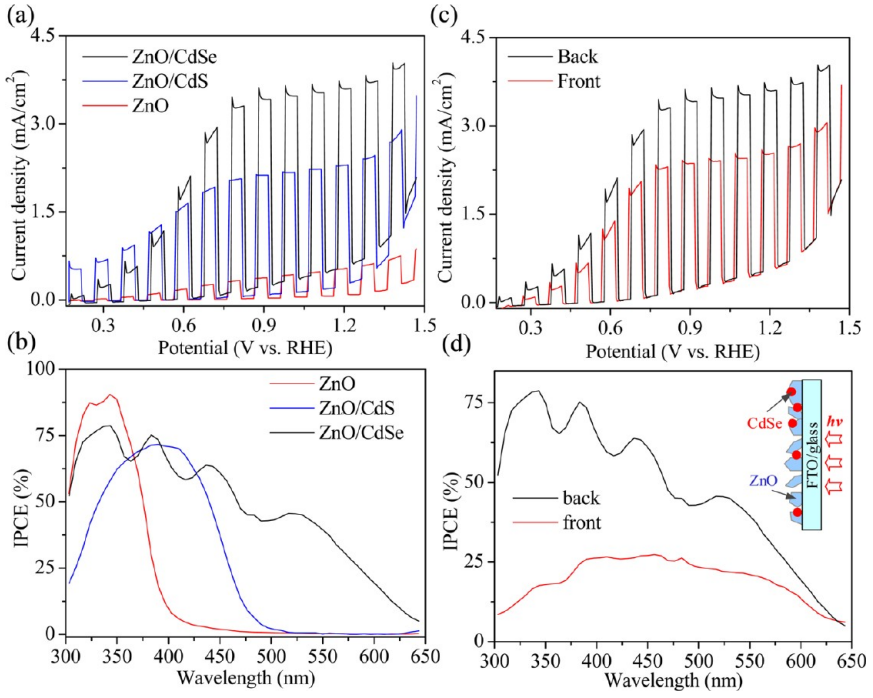

Figure 7. (a) *I*–*V* characteristics and (b) IPCE spectra of pure ZnO and CdX-sensitized ZnO electrodes (X = S, Se) under one sun (AM1.5, 100 mW/cm^2) illumination and chopped light (illumination from back side). (c) *I*–*V* characteristics and (d) IPCE spectra of ZnO/CdSe samples measured in front and back configurations (sample used in panels (a) and (b)). The IPCE spectra were taken with bias at 1.23 V vs RHE. The inset in panel (d) is a scheme of an electrode illuminated from the back side.

front and back illumination, but this can be ruled out (see the Supporting Information).

Based on the IPCE values and solar spectrum under standardized conditions (AM 1.5 G), the total photocurrent that would be expected for a PEC can be estimated (see the Supporting Information). The calculated photocurrent density for the CdSe-sensitized ZnO electrodes is 6.5 mA/cm^2. This value is much higher than that obtained for the ZnO and ZnO/CdS electrodes, which are 0.9 and 2.5 mA/cm^2, respectively. Comparing the experimentally determined and the integrated photocurrent densities of the ZnO/CdSe electrode, ~50% of the predicted photocurrent is obtained. This difference indicates that recombination increases at higher light intensities. This may be due to either slow surface reaction kinetics or mass transport limitations in the electrolyte phase within the mesoporous structure. Further optimization of ZnO plate density on the FTO substrate is expected to increase the photocurrent higher than ~3.1 mA/cm^2.

Figure 8 shows a schematic of the PEC used in our studies, combined with an energy level alignment of ZnO and CdX (X = S, Se) systems. It is well-known that when ZnO is in contact with CdSe, it makes a type-II band gap alignment, which means the conduction band edge of ZnO is located between the conduction band and the valence band of CdSe.[13] In this band-gap configuration, when electron–hole pairs are generated by VIS light excitation in CdSe nanoparticles, the photoelectrons (e^-) can be transferred to the conduction band of the ZnO plate, which facilitates the charge separation process of electron–hole pairs before they recombine. The photo-generated holes (h^+), which remain in the CdSe, will react with the species in the surrounding electrolyte. It is known that cadmium chalcogenides (e.g., CdS, CdSe) are not stable in aqueous solutions under irradiation due to the anodic dissolution; such a disadvantage can be avoided in the presence

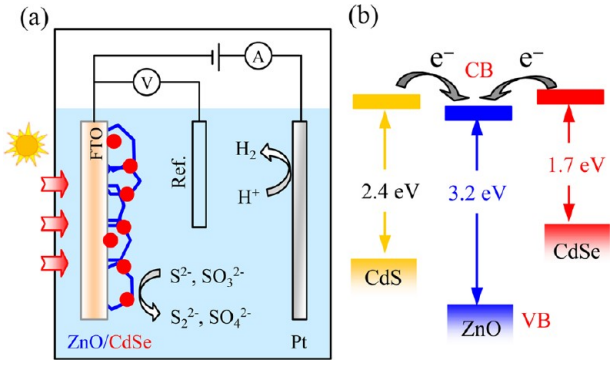

Figure 8. (a) Scheme of ZnO/CdSe PEC. (b) Conduction band (CB) and valence band (VB) positions for bulk semiconductor ZnO, CdS, and CdSe.[42].

of sacrificial reagents of S^{2-} and SO_3^{2-}. In the present case, the photogenerated holes reacts with the S^{2-} and SO_3^{2-} species. The possible mechanisms for the reactions taking place on the Pt cathode and ZnO/CdSe photoanode can be summarized as follows:[14,61–64]

$$\text{photocatalyst} + h\nu \rightarrow e^-(\text{CB}) + h^+(\text{VB}) \quad (6)$$

$$2H_2O + 2e^-(\text{CB}) \rightarrow H_2 + 2OH^- \quad (7)$$

$$SO_3^{2-} + 2OH^- + 2h^+(\text{VB}) \rightarrow SO_4^{2-} + H_2O \quad (8)$$

$$2S^{2-} + 2h^+(\text{VB}) \rightarrow S_2^{2-} \quad (9)$$

$$2SO_3^{2-} + 2h^+ \rightarrow S_2O_6^{2-} \quad (10)$$

$$S_2^{2-} + S_3^{2-} \rightarrow S_2O_3^{2-} + S^{2-} \quad (11)$$

$$SO_3^{2-} + S^{2-} + 2h^+(VB) \rightarrow S_2O_3^{3-} \quad (12)$$

$$0.5S_2O_3^{2-} + 1.5H_2O + 2h^+(VB) \rightarrow SO_3^{2-} + 3H^+ \quad (13)$$

The photogenerated holes in the valence band oxidize SO_3^{2-} and S^{2-} to form SO_4^{2-} and S_2^{2-}. The production of S_2^{2-} is efficiently suppressed by its reaction with SO_3^{2-}. Moreover, the presence of excess S^{2-} ions in the reaction solution can stabilize the photocatalyst (e.g., CdS) surface because the formation of surface defects could be suppressed. Since $S_2O_3^{2-}$ could also be oxidized to SO_3^{2-} and subsequently to SO_4^{2-} by the photogenerated holes, it has also been used as a sacrificial agent.[65,66] We can expect that the generated photocurrent by the PEC will be stable as long as there are enough species of S^{2-} and SO_3^{2-}. After the consumption of these species, photodissolution may take place in the QDs, which eventually may result in a decrease in current. Since we did not purge the electrolyte solution with inert gas, some side reactions with dissolved oxygen gas may occur (see the Supporting Information). However, since the amount of dissolved oxygen is much smaller than the concentration of S_2 and SO_3^{2-}, we believe this plays a minor role.

Electrochemical Impedance Spectroscopy (EIS) Studies of ZnO and ZnO/CdSe Electrodes. EIS is a powerful technique utilized to investigate the processes that occur at an electrode/liquid interface.[67,68] To analyze the characteristics of charge transfer in PECs, EIS studies were conducted at 0.51 V (vs RHE) under AM1.5 illumination in the frequency range of $1-10^4$ Hz. Figure 9 presents typical Nyquist plots of ZnO and ZnO/CdSe electrodes. As can be seen from this plot, there is a distinct difference in the electrochemical behavior between the ZnO and ZnO/CdSe samples. The arc with its maximum in the low-frequency region is due to the contribution from electron transport resistance (R_1) in ZnO or ZnO/CdSe electrodes. A smaller arc is obtained for the ZnO/CdSe electrode. To determine the reason for this disparity, we fitted the EIS data by using the simple circuit-element shown in Figure 9. The results are presented in Table 1. The R_1 value of the ZnO/CdSe cell is ~4000 Ω, which is much lower than that for the ZnO cell (13 000 Ω), which represents faster hole transfer kinetics for the ZnO/CdSe cells. This, we believe, is also an additional factor contributing to higher photocurrents observed in the CdSe/ZnO electrode.

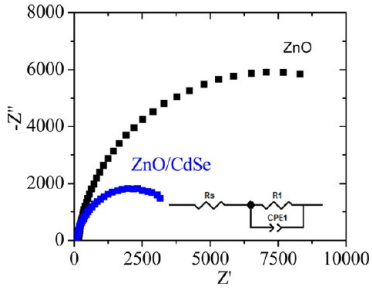

Figure 9. Nyquist plot of impedance spectra measured at a bias of 0.51 V vs RHE under AM1.5 G (100 mW/cm^2) illumination. Frequency range = $1-10^4$ Hz. Inset shows the equivalent circuit used to model the EIS data.

Stability of CdSe-sensitized ZnO Plate Electrodes. The stability issues associated with QDs are one of the obstacles in realizing PECs based on II–VI semiconductors such as CdS, CdSe, PbS, etc. We try to address this issue, by illumination of PEC system for prolonged duration. By recording the photocurrent density (J) as a function of illumination time, we were able to get an idea of the stability of our photoanode electrodes. Figure 10 shows the change in J versus time upon illumination of the ZnO/CdSe electrode. We studied the stability of this electrode in the presence and absence of a sacrificial electron donor (SED). When we used a SED (0.1 M Na_2S/0.1 M Na_2SO_3) as an electrolyte for these PEC studies, we found that the solution was basic (pH 13). In order to reproduce the same conditions (but without the SED), we also measured the stability in an aqueous NaOH solution (pH 13). As shown in Figure 10, the photocurrent density of the ZnO/CdSe electrodes drastically decreased in the NaOH solution, whereas significant stability was observed in the presence of a SED. The degradation of the material in the NaOH solution is due to photoanodic dissolution of the CdSe.[69] The addition of a SED prevents this through efficient regeneration of the oxidized CdSe (h^+) QDs. The presence of SED almost completely prevents decomposition of CdSe QDs (Figure 10). To further improve the stability of the ZnO/CdSe electrodes, surface passivation with ultrathin protective coatings[70] or the deposition of co-catalyst[71] on the CdSe particles seems a promising strategy for the development of stable cadmium chalcogenide-based photoelectrodes.

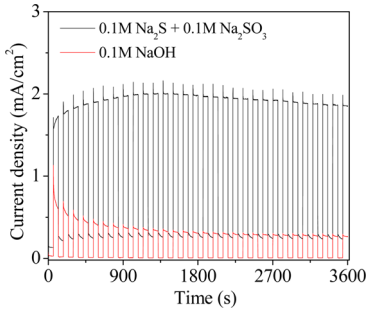

Figure 10. Photocurrent performance at 1.23 V (vs NHE) of CdSe-sensitized porous ZnO electrodes in a mixture of 0.1 M Na_2S/0.1 M Na_2SO_3 (black) and 0.1 M NaOH (red) solutions using periodic illumination intervals. The cell is illuminated in back configuration.

4. CONCLUSIONS

In summary, by employing a facile electrochemical method, we have prepared porous ZnO films with a platelike morphology. We used these porous ZnO electrodes in photoelectrochemical (PEC) studies. Because of the limited absorption of ZnO in the

Table 1. Equivalent-Circuit Fitting Parameters

system	series resistance, R_s (Ω)	resistance in ZnO or ZnO/CdX, R_1 (Ω)	CPE_1T ($\times 10^{-6}$)^a	CPE_1P^a	frequency, f_{max} (Hz)	$C_1{}^b$ ($\times 10^{-6}$ F)
ZnO	153.1	12920	9.982	0.93	1.41	8.6
ZnO/CdSe	93.6	4005	22.76	0.93	2.26	19

^{a}CPE = constant phase element. $^b C_1 = CPE_1T \times (2\pi f_{max})^{(CPE_1P-1)}$.

dx.doi.org/10.1021/am3027986 | ACS Appl. Mater. Interfaces 2013, 5, 1113–1121

visible (VIS) range, we used CdX (X = S, Se) QDs to sensitize the ZnO films. As a result of this sensitization we obtained visible-light photoactive electrodes. Detailed PEC studies confirmed that the CdSe-sensitized ZnO electrode shows the highest photocurrent, because of the superior light-harvesting efficiency of this material. While the photocurrent of our system is currently still smaller than other reports on CdX-sensitized ZnO nanostructures (see refs 28−32, 39, 40, 42, and 43), the preparation of ZnO films with platelike morphology provides an alternative way of texturing ZnO and for the development of visible-light responsive photoelectrodes for photoelectrochemical and photovoltaic applications.

■ ASSOCIATED CONTENT

Supporting Information

SEM data and details on density of ZnO plates. Calculation of photocurrent density. This material is available free of charge via the Internet at http://pubs.acs.org.

■ AUTHOR INFORMATION

Corresponding Author

*Tel.: +38/(0)653653502. Fax: +386/(0)53653527. E-mails: Saim.Emin@ung.si, eminsaim@yahoo.com.

Notes

The authors declare no competing financial interest.

■ ACKNOWLEDGMENTS

The authors acknowledge the Slovenian Research Agency for funding this research, under Grant Nos. N2-0005-1540 and P2-0089. S. E. thanks the support of the European Commission under the Marie Curie Career Integration Grant (HETMAT, Project 322114). F.F.A. gratefully acknowledges European Commission's Framework Project 7 (NanoPEC, Project No. 227179) for financial support. We thank to CENN for the use of their TEM, Centre of Excellence for Biosensors, Instrumentation and Process Control for use of their XRD and Lab. TASC, IOM-CNR for the use of their SEM.

■ REFERENCES

(1) Wagata, H.; Katsumata, K.; Ohashi, N.; Sakai, M.; Nakajima, A.; Fujishima, A.; Okada, K.; Matsushita, N. *Photochem. Photobiol.* **2011**, *87*, 1009−1015.
(2) Xu, F.; Dai, M.; Lu, Y.; Sun, L. *J. Phys. Chem. C* **2010**, *114*, 2776−2782.
(3) Qiu, Y.; Yan, K.; Deng, H.; Yang, S. *Nano Lett.* **2012**, *12*, 407−413.
(4) Lopez, C. M.; Choi, K.-S. *Chem. Commun.* **2005**, 3328−3330.
(5) Park, S. K.; Park, J. H.; Ko, K. Y.; Yoon, S.; Chu, K. S.; Kim, W.; Do, Y. R. *Cryst. Growth Des.* **2009**, *9*, 3615−3620.
(6) Xu, F.; Lu, Y.; Xie, Y.; Liu, Y. *Mater. Des.* **2009**, *30*, 1704−1711.
(7) Xu, C.; Gao, D. *J. Phys. Chem. C* **2012**, *116*, 7236−7241.
(8) Cheng, H-.M.; Chiu, W.-H.; Lee, C.-H.; Tsai, S.-Y.; Hsieh, W.-F. *J. Phys. Chem. C* **2008**, *112*, 16359−16364.
(9) Ko, S. H.; Lee, D.; Kang, H. W.; Yeo, J. Y.; Hong, S. J.; Grigoropoulos, C. P.; Sung, H. J. *Nano Lett.* **2011**, *11*, 666−671.
(10) Wang, J. X.; Wu, C. M. L.; Cheung, W. S.; Luo, L. B.; He, Z. B.; Yuan, G. D.; Zhang, W. J.; Lee, C. S.; Lee, S. T. *J. Phys. Chem. C* **2010**, *114*, 13157−13161.
(11) Barpuzary, D.; Khan, Z.; Vinothkumar, N.; De, M.; Qureshi, M. *J. Phys. Chem. C* **2012**, *116*, 150−156.
(12) Chen, H.; Li, W.; Liu, H.; Zhu, L. *Electrochem. Commun.* **2011**, *13*, 331−334.
(13) Wang, H.; Wang, T.; Wang, X.; Liu, R.; Wang, B.; Wang, H.; Xu, Y.; Zhang, J.; Duan, J. *J. Mater. Chem.* **2012**, *22*, 12532−12537.
(14) Kim, H.; Seol, M.; Lee, J.; Yong, K. *J. Phys. Chem. C* **2011**, *115*, 25429−25436.
(15) Seol, M.; Kim, H.; Tak, Y.; Yong, K. *Chem. Commun.* **2010**, *46*, 5521−5523.
(16) Cao, X.; Chen, P.; Guo, Y. *J. Phys. Chem. C* **2008**, *112*, 20560−20566.
(17) Sarkar, S.; Makhal, A.; Lakshman, K.; Bora, T.; Dutta, J.; Pal, S. K. *J. Phys. Chem. C* **2012**, *116*, 14248−14256.
(18) Murphy, C. J.; Coffer, J. L. *Appl. Spectrosc.* **2002**, *56*, 16−27.
(19) Emin, S.; Singh, S. P.; Han, L.; Satoh, N.; Islam, A. *Sol. Energy* **2011**, *85*, 1264−1282.
(20) Wang, C.; Thompson, R. L.; Ohodnicki, P.; Baltrus, J.; Matranga, C. *J. Mater. Chem.* **2011**, *11*, 13452−13457.
(21) Baskoutas, S.; Terzis, A. F. *J. Appl. Phys.* **2006**, *99*, 013708.
(22) Tang, Z.; Zhang, Z.; Wang, Y.; Glotzer, S. C.; Kotov, N. A. *Science* **2006**, *314*, 274−278.
(23) Pan, Z.; Zhang, H.; Cheng, K.; Hou, Y.; Hua, J.; Zhong, X. *ACS Nano* **2012**, *6*, 3982−3991.
(24) Lin, S.-C.; Lee, Y.-L.; Chang, C.-H.; Shen, Y.-J.; Yang, Y.-M. *Appl. Phys. Lett.* **2007**, *90*, 1435171.
(25) Shen, Q.; Toyoda, T. *Jpn. J. Appl. Phys.* **2004**, *43*, 2946−2951.
(26) Emin, S.; Yanagida, M.; Peng, W.; Han, L. *Sol. Energy Mater. Sol. Cells* **2012**, *101*, 5−10.
(27) Luo, J.; Karaturi, S. K.; Liu, L.; Su, L. T.; Tok, A. L. Y.; Fan, H. *J. Sci. Rep.* **2012**, *2*, 451.
(28) Qi, X.; She, G.; Liu, Y.; Mu, L.; Shi, W. *Chem. Commun.* **2012**, *48*, 242−244.
(29) Tak, Y.; Hong, S. J.; Lee, J. S.; Yong, K. *J. Mater. Chem.* **2009**, *19*, 5945−5945.
(30) Mane, R. S.; Shinde, D. V.; Yoon, S. J.; Ambade, S. B.; Lee, J. K.; Han, S.-H. *Appl. Phys. Lett.* **2012**, *101*, 033906.
(31) Leschkies, K. S.; Divakar, R.; Basu, J.; Enache-Pommer, E.; Boercker, J. E.; Carter, C. B.; Kortshagen, U. R.; Norris, D. J.; Aydil, E. S. *Nano Lett.* **2007**, *7*, 1793−1798.
(32) Xu, J.; Yang, X.; Yang, Q.-D.; Wong, T.-L.; Lee, S.-T.; Zhang, W.-J.; Lee, C.-S. *J. Mater. Chem.* **2012**, *22*, 13374−13379.
(33) Chen, H. M.; Chen, C. K.; Chang, Y.-C.; Tsai, C.-W.; Liu, R.-S.; Hu, S.-F.; Chang, W.-S.; Chen, K.-H. *Angew. Chem., Int. Ed.* **2010**, *49*, 5966−5969.
(34) Li, T.-L.; Lee, Y.-L.; Teng, H. *J. Mater. Chem.* **2011**, *21*, 5089−5098.
(35) Li, H.; Cheng, C.; Li, X.; Liu, J.; Guang, C.; Tay, Y. Y.; Fan, H. J. *J. Phys. Chem. C* **2011**, *116*, 3802−3807.
(36) Ladanov, M.; Ram, M. K.; Matthews, G.; Kumar, A. *Langmuir* **2011**, *27*, 9012−9017.
(37) Du, J.; Qi, J.; Wang, D.; Tang, Z. *Energy Environ. Sci.* **2012**, *5*, 6914−6918.
(38) Chen, J.; Wu, J.; Lei, W.; Song, J. L.; Deng, W. Q.; Sun, X. W. *Appl. Surf. Sci.* **2010**, *256*, 7438−7441.
(39) Chen, Y.; Wei, L.; Zhang, G.; Jiao, J. *Nanoscale Res. Lett.* **2012**, *7*, 516.
(40) Sudhagar, P.; Song, T.; Lee, D. H.; Mora-Sero, I.; Bisquert, J.; Laudenslager, M.; Sigmund, W. M.; Park, W. I.; Paik, U.; Kang, Y. S. *J. Phys. Chem. Lett.* **2011**, *2*, 1984−1990.
(41) Zhang, R.; Luo, Q. P.; Chen, H.-Y.; Yu, X.-Y.; Kuang, D.-B.; Su, C.-Y. *Chem. Phys. Chem.* **2012**, *13*, 1435−1439.
(42) Wang, G.; Yang, X.; Qian, F.; Zhang, J. Z.; Li, Y. *Nano Lett.* **2010**, *10*, 1088−1092.
(43) Myung, Y.; Jang, D. M.; Sung, T. K.; Sohn, Y. J.; Jung, G. B.; Cho, Y. J.; Kim, H. S.; Park, J. *ACS Nano* **2010**, *4*, 3789−3800.
(44) Wei, X.; Ke, L.; Kong, J.; Liu, Hong; Jiao, Z.; Lu, X.; Du, H.; Sun, X. W. *Nanotechnology* **2012**, *23*, 235401.
(45) Taleatu, B. A.; Fasasi, A. Y.; Di santo, G.; Bernstorff, S.; Goldoni, A.; Fanetti, M.; Floreano, L.; Borghetti, P.; Casalis, L.; Sanavio, B.; Castellarin-Cudia, C. *AIP Adv.* **2011**, *1*, 032147.
(46) Hoang, S.; Guo, S.; Hahn, N. T.; Bard, A. J.; Mullins, C. B. *Nano Lett.* **2011**, *12*, 26−32.
(47) Moss, J. A.; Yang, J. C.; Stipkala, J. M.; Wen, X.; Bignozzi, C. A.; Meyer, G. J.; Meyer, T. *J. Inorg. Chem.* **2004**, *43*, 1784−1794.

(48) Long, T.; Yin, S.; Takabatake, K.; Zhang, P.; Sato, T. *Nanoscale Res. Lett.* **2009**, *4*, 247−253.
(49) Sheini, F. J.; Singh, J.; Srivastava, O. N.; Joag, D. S.; More, M. A. *Appl. Surf. Sci.* **2010**, *256*, 2110−2114.
(50) Schmetzer, K.; Schnorrer-Kohler, G.; Molenbach, O. *Neues Jahrb. Mineral. Monatsh.* **1985**, 145−154.
(51) Sawada, H.; Wang, R.; Sleight, A. W. *J. Solid State Chem.* **1996**, *122*, 148−150.
(52) Emin, S.; Lisjak, D.; Pitcher, M.; Valant, M. *Microporous Mesoporous Mater.* **2013**, *165*, 185−192.
(53) Srivastava, O. K.; Secco, E. A. *Can. J. Chem.* **1967**, *45*, 579−583.
(54) Dong, Z.; Lai, X.; Halpert, E. J.; Yang, N.; Yi, L.; Zhai, J.; Wang, D.; Tang, Z.; Jiang, L. *Adv. Mater.* **2012**, *24*, 1046−1049.
(55) Wang, L.; Zhao, D.; Su, Z.; Shen, D. *Nanoscale Res. Lett.* **2012**, *7*, 106.
(56) Foresti, M. L.; Milani, S.; Loglio, F.; Innocenti, M.; Pezzatini, G.; Cattarin, S. *Langmuir* **2005**, *21*, 6900−6907.
(57) Smith, A. M.; Nie, S. *Acc. Chem. Res.* **2010**, *43*, 190−200.
(58) Abdi, F. F.; van de Krol, R. *J. Phys. Chem C* **2012**, *116*, 9398−9404.
(59) Riha, S. C.; Frederick, S. J.; Sambur, J. B.; Liu, Y.; Prieto, A. L.; Parkinson, B. A. *ACS Appl. Mater. Interfaces* **2011**, *3*, 58−66.
(60) Liang, Y.; Tsubota, T.; Mooij, L. P. A.; van de Krol, R. *J. Phys. Chem. C* **2011**, *115*, 17594−17598.
(61) Tsuji, I.; Kato, H.; Kobayashi, H.; Kudo, A. *J. Am. Chem. Soc.* **2004**, *126*, 13406−13413.
(62) Banerjee, S.; Mohapatra, K.; Das, P. P.; Misra, M. *Chem. Mater.* **2008**, *20*, 6784−6791.
(63) Chen, X.; Shen, S.; Guo, L.; Mao, S. S. *Chem. Rev.* **2010**, *110*, 6503−6570.
(64) Chai, B.; Peng, T.; Zeng, P.; Zhang, X.; Liu, X. *J. Phys. Chem. C* **2011**, *115*, 6149−6155.
(65) Brahimi, R.; Bessekhouad, Y.; Bouguelia, A.; Trari, M. *J. Photochem. Photobiol. A* **2007**, *186*, 242−247.
(66) Derbal, A.; Omeiri, S.; Bouguelia, A.; Trari, M. *Int. J. Hydrogen Energy* **2008**, *33*, 4274−4282.
(67) Chen, J.; Li, C.; Zhao, D. W.; Zhang, Y.; Cole, M. T.; Wang, B. P.; Cui, Y. P.; Sun, X. W.; Milne, W. I. *Electrochem. Soc.* **2010**, *12*, 1432−1435.
(68) Yu, X.-Y.; Liao, J.-Y.; Qiu, K.-Q.; Kuang, D.-B.; Su, C.-Y. *ACS Nano* **2012**, *5*, 9494−9500.
(69) Ellis, A. B.; Kaiser, S. W.; Bolts, J. M.; Wrighton, M. S. *J. Am. Chem. Soc.* **1977**, *99*, 2839−2848.
(70) Paracchino, A.; Laporte, V.; Sivula, K.; Gratzel, M.; Thimsen, E. *Nat. Mater.* **2011**, *10*, 456−461.
(71) Li, Y.; Takata, T.; Cha, D.; Takanabe, K.; Minegishi, T.; Kubota, J.; Domen, K. *Adv. Mater.* **2012**, DOI: 10.1002/adma.201202582.